

Organic Electrochemical Transistor-Based Immunosensors for SARS-CoV-2 Detection

Renan Colucci,* Dimitrios A. Koutsouras, Svenja Morsbach, Paschalis Gkoupidenis, Paul W. M. Blom, and Ulrike Kraft*

Cite This: *ACS Appl. Electron. Mater.* 2024, 6, 2739–2748

Read Online

ACCESS |

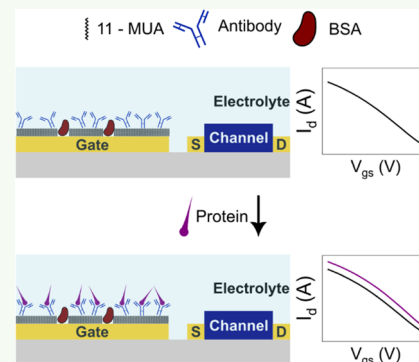
Metrics & More

Article Recommendations

Supporting Information

ABSTRACT: Following the emergence of the worldwide severe respiratory syndrome coronavirus 2 (SARS-CoV-2) pandemic, the need for innovative strategies and methodologies to facilitate cost-effective and early stage diagnosis has become evident. To prevent the outbreak of such contagious diseases, an efficient approach is systematic testing of the population. Here, we introduce a planar organic electrochemical transistor (OECT)-based immunosensor for the detection of SARS-CoV-2. The gold gate electrode of the poly(3,4-ethylenedioxy-thiophene):polystyrene sulfonate (PEDOT:PSS)-based OECTs was functionalized with SARS-CoV-2 antibodies. The detection mechanism is based on the specific interaction of the antibodies with the spike protein of the virus, allowing its direct detection and not requiring the prior formation of antibodies in the patient's body. As a proof of concept, the ability of the immunosensor to detect the SARS-CoV-2 spike protein is assessed. The sensor exhibits a remarkably low limit of detection (LOD) of 10^{-17} M, with an incubation time of 30 min. Furthermore, the sensors demonstrate selectivity when exposed to similar proteins and stability, retaining their LOD after 20 days of storage. Lastly, the functionalization protocol may easily be adapted for other pathogens/biomarkers, enabling not only a point-of-care device for SARS-CoV-2 detection but also a versatile platform for biosensing applications.

KEYWORDS: OECT, PEDOT:PSS, biosensor, immunosensor, SARS-CoV-2



but also for transferable to various diseases including potential future viruses. Electronic biosensors have emerged as devices capable of addressing these demands. Typically, a biosensor consists of a bioreceptor that interacts with the analyte (antigen) to be analyzed and a transducer that converts such biological incident into a measurable one.⁷ Organic electrochemical transistors (OECTs) have shown highly promising results as they combine transducing and signal amplification abilities.^{8,9} OECTs are three-terminal devices comprised of an organic mixed conductor film (channel) in contact with two electrodes, namely, source and drain. The channel of the OECT in turn interfaces with an electrolyte, in which the third electrode, the gate, is immersed. During operation, the gate voltage drives ions from the electrolyte in and out of the channel, causing electrochemical reactions that (de) dope the channel and thereby modulate its electronic conductivity.^{10,11} In other words, the OECTs have the ability to convert ionic fluxes into electronic signals. Unlike traditional field effect

INTRODUCTION

The World Health Organization (WHO) classified the outbreak of the severe respiratory syndrome coronavirus 2 (SARS-CoV-2) as a global pandemic in early 2020.¹ The rapidly transmitted SARS-CoV-2 has severely affected society and global health. Quick, reliable, transferable, and easy-to-handle point-of-care (POC) testing strategies with a low limit of detection (LOD) are crucial to halting the spread of such viruses. Currently, the gold standard method to detect contaminated patients is reverse transcription-quantitative polymerase chain reaction (RT-qPCR). RT-qPCR detects the genetic material of the virus by amplifying specific target sequences using polymerase chain reaction (PCR) technology. This method provides high sensitivity, meaning it can detect even small amounts of viral genetic material in a sample. However, it does require trained personnel, specialized equipment, and high-quality samples to ensure accurate results, and it is time-consuming, which makes it incompatible with POC device applications.^{2–4} An alternative to the RT-qPCR suitable as a POC device is the viral antigen test (rapid test). It provides a rapid result (~30 min), however lacks sensitivity, which generates a high number of false-negative results.^{5,6}

Therefore, there is a pressing need for innovative approaches and methodologies to enable low-cost and early stage diagnosis, ideally, not only for the detection of SARS-CoV-2

but also for transferable to various diseases including potential future viruses. Electronic biosensors have emerged as devices capable of addressing these demands. Typically, a biosensor consists of a bioreceptor that interacts with the analyte (antigen) to be analyzed and a transducer that converts such biological incident into a measurable one.⁷ Organic electrochemical transistors (OECTs) have shown highly promising results as they combine transducing and signal amplification abilities.^{8,9} OECTs are three-terminal devices comprised of an organic mixed conductor film (channel) in contact with two electrodes, namely, source and drain. The channel of the OECT in turn interfaces with an electrolyte, in which the third electrode, the gate, is immersed. During operation, the gate voltage drives ions from the electrolyte in and out of the channel, causing electrochemical reactions that (de) dope the channel and thereby modulate its electronic conductivity.^{10,11} In other words, the OECTs have the ability to convert ionic fluxes into electronic signals. Unlike traditional field effect

Received: February 9, 2024

Revised: March 15, 2024

Accepted: March 18, 2024

Published: March 29, 2024



transistors, OECTs possess a distinct advantage in terms of transconductance and hence signal amplification due to the accumulation of ions throughout the entire volume of the channel. Furthermore, OECTs offer biocompatibility, operate in aqueous environments at low potentials (typically < 111 V), and exhibit high stability, in addition to being a self-amplification device.^{12,13} Recent applications of OECTs as biosensors include the detection of enzymes,^{14–16} proteins,^{17,18} bacteria,^{19,20} viruses,^{21,22} and genetic materials.²³

In the context of using the OECTs as transducers for SARS-CoV-2 detection, the available literature is still limited, but some notable studies have emerged. For example, a study conducted by Guo et al.²¹ introduced an OECT-based biosensor, where nanobodies were immobilized onto the gold gate electrode in order to detect the SARS-CoV-2 spike protein. The authors investigated two distinct channel materials, namely, p(gOT2-g6T2) and poly(3,4-ethylenedioxythiophene):poly(styrene sulfonate) (PEDOT:PSS). In another study, Liu et al.²⁴ reported the development of a PEDOT:PSS-based OECT biosensor that specifically targeted the detection of SARS-CoV-2 spike antibodies and employed the SARS-CoV-2 spike protein as a bioreceptor, which was immobilized on the gold gate surface. These studies employed different channel materials, device architectures, and bioreceptor-antigen interactions to fabricate a first generation of highly sensitive and selective sensors for SARS-CoV-2 detection. However, alternative strategies and further optimization will enhance the performance of the OECT-based sensors to meet the demand for low LOD, improved stability, and simplified fabrication. Such strategies include modifications to the OECT, optimized device architectures, and advancements in the functionalization procedure.

In this study, we introduce a novel approach toward a PEDOT:PSS-based OECT immunosensor for the detection of SARS-CoV-2. The Au gate electrode is functionalized by immobilizing the SARS-CoV-2 spike antibody (Ab) through covalent bonding. This approach allows the direct detection of SARS-CoV-2 without the prior formation of antibodies in the patient's body. In this specific study, however, we first focus on the detection of the respective SARS-CoV-2 spike protein for safety precautions. To serve as an intermediate binding layer between the Ab and Au gate electrodes, a self-assembled monolayer (SAM) of 11-mercaptoundecanoic acid (11MUA), an alkanethiol, is utilized. Remarkably, our device exhibits an exceptional capability to detect the SARS-CoV-2 spike protein with an extremely low LOD of 10^{-17} M. Furthermore, the immunosensors exhibit specificity, as demonstrated by their minimal response to bovine serum albumin (BSA) and Middle East respiratory syndrome coronavirus (MERS-CoV) spike protein. Moreover, the devices exhibit very good stability during storage, as the sensors retain their functionality and properties, even after being stored for several weeks. Overall, this PEDOT:PSS-based OECT immunosensor is a highly sensitive, specific, and stable device for the detection of the SARS-CoV-2 spike protein, offering promising prospects for applications in diagnostics such as POC.

EXPERIMENTAL SECTION

Materials. 11-Mercaptoundecanoic acid (11MUA), *N*-(3-(dimethylamino)propyl)-*N'*-ethyl-carbodiimide (EDC), *N*-hydroxysuccinimide (NHS), bovine serum albumin (BSA), phosphate-buffered saline (PBS) (pH 7.2), artificial saliva, human serum type

AB, ethylene glycol, 4-dodecylbenzenesulfonic acid (DBSA), (3-glycidyloxypropyl)trimethoxysilane (GOPS), potassium hexacyanoferrate (II) trihydrate, and potassium hexacyanoferrate (III) were all purchased from Sigma-Aldrich Co. SARS-CoV-2 spike protein (S1, Fc tag C-Terminus; molecular weight—140 kDa, ab272105) and SARS-CoV-2 IgG (S1 Spike antibody; molecular weight—150 kDa, ab273073) were purchased from ABCAM, Germany. MERS-CoV Spike/Spike protein (S1 Subunit, aa 1-725, His-Tag, 40069-V08H) was purchased from Sino Biological. Poly(3,4-ethylenedioxythiophene):poly(styrene sulfonate) (PEDOT:PSS) (Clevios PH1000) aqueous solution was purchased from Heraeus Ltd.

PEDOT:PSS OECT Formulation. The PEDOT:PSS formulation for the fabrication of the OECT consists of 38 mL of PEDOT:PSS, 2 mL of ethylene glycol (to increase the conductivity), 0.4 mL of GOPS (acting as a cross-linker agent), and 50 μ L of DBSA (to facilitate film formation).

Device Fabrication. The devices were fabricated using a similar protocol reported by Koutsouras et al.²⁵ First, the drain, source, and gate electrodes made of Cr/Au (10/100 nm) were patterned on optical microscope glass slides (26 \times 76 mm) using photolithography. Subsequently, to precisely define the channel and gate regions, the devices were encapsulated with double parylene C layers. The first layer served as an isolating layer, while the second served as a sacrificial one. Following substrate encapsulation, the regions of the gate electrodes and the transistors' channels were patterned by photolithography. Finally, reactive ion etching (RIE) with O₂ plasma was employed to remove parylene C under these regions and to expose the Au electrodes and the device channel.

The PEDOT:PSS OECT formulation was spin-coated onto the devices at 3000 rpm for 60 s and hard baked at 140 °C for an hour. Subsequently, the OECTs were soaked in distilled water overnight to remove excess low-molecular-weight molecules from the channel. The fabricated OECTs had a channel length of 1 mm, a channel width of 0.3 mm (W \times L), an average PEDOT:PSS thickness of 55 ± 5 nm, and a 4 mm diameter gate electrode.

Gate Functionalization. After formation of the PEDOT:PSS channel, the Au gate electrodes were cleaned with a 1:1 (v/v) solvent mixture (acetone/isopropyl alcohol) in a sonication bath. The cleaned Au electrodes were immersed in an 11MUA (10 mM) ethanol solution overnight to allow the formation of a self-assembled monolayer (SAM) with functional carboxylic groups. The latter were activated afterward in a mixed solution of EDC (20 mM) and NHS (10 mM) in MES for 30 min. During these last steps, only the gold gate electrode was immersed in the solvent/solutions, preventing any contamination of the PEDOT:PSS channel. Afterward, the gate electrodes were covered by a 150 μ L SARS-CoV-2 antibodies solution (10^{-8} M in PBS solution) for 30 min. The antibodies were then attached to the SAM through the formation of covalent bonds between their amine groups and the activated carboxylic groups. The applied antibody concentration is within the reported literature range (10^{-11} – 10^{-7} M).^{26–28} We selected a concentration to ensure enough antibodies for full coverage on our gate electrode considering the solution volume. The chosen incubation time was based on the presented QCM-D results. In order to prevent any remaining nonspecific binding sites on the Au electrode, the devices were submerged in a BSA solution (10 mg mL⁻¹) for a duration of 30 min.

OECT Characterization and Sensor Operation. The functionalized gate electrodes underwent a 30 min incubation period with a 150 μ L solution of SARS-CoV-2 spike protein, BSA, or MERS-CoV spike protein, each at the respective concentration, diluted in PBS. Additionally, the SARS-CoV-2 spike protein was also diluted in artificial saliva and human serum for further assessment. After each step of functionalization, the gate electrodes were rinsed thoroughly in water and gently dried with nitrogen to remove possible residues. A poly(dimethylsiloxane) (PDMS) well was used to hold the PBS electrolyte over the gate and channel. The electrical measurements were performed using a Keithley 4200A-SCS. All fresh devices were subjected to a precycling of a series of 10 output measurements within a V_{gs} range of -0.5 V to 0.5 V (0.1 V steps) and V_{ds} ranging from 0.05 to

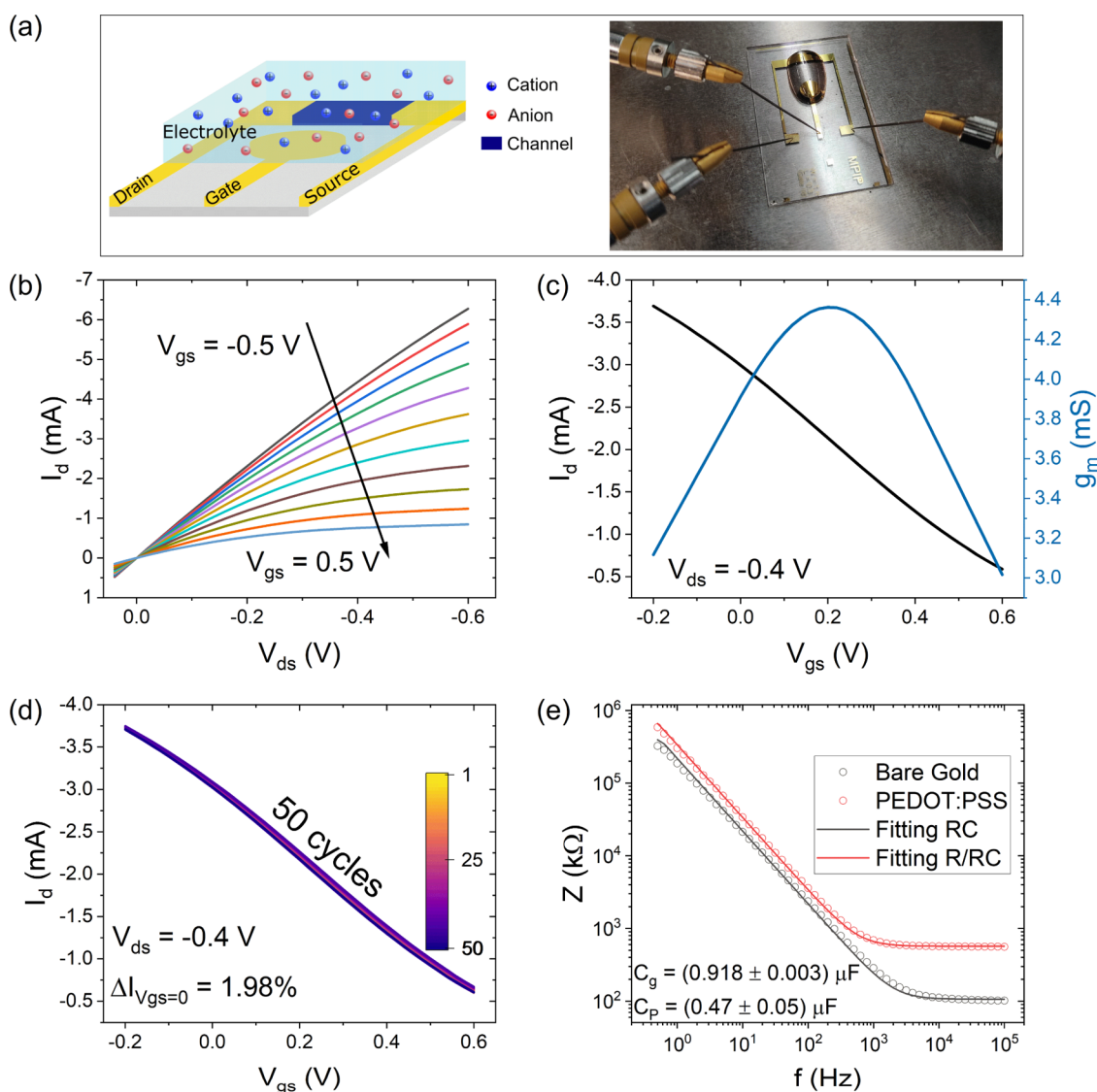


Figure 1. (a) Left: sketch of a typical planar organic electrochemical transistor (OECT). Right: photograph of a representative planar OECT used in this work. (b) Family of output curves. (c) Transfer curve and transconductance for $V_{ds} = -0.4$ V. (d) Stability of the device during 50 consecutive transfer curve cycles at $V_{ds} = -0.4$ V. (e) Electrochemical impedance spectroscopy (EIS) of the bare Au gate electrode and the PEDOT:PSS channel. All results were obtained for devices with channel dimension of 1×0.3 mm (W \times L), with an average PEDOT:PSS thickness of 55 ± 5 nm and a Au gate electrode of 4 mm of diameter. All measurements were performed using PBS solution as the electrolyte.

-0.6 V and a series of 10 transfer cycles with V_{ds} stepping from -0.2 to -0.6 V (-0.2 V steps) and V_{gs} ranging from -0.2 to 0.6 V. For the sensor tests, for each change of the protein concentration, the steady-state transistor characteristics were obtained cycling the devices for 5 families of output and transfer curves.

Sensor Characterization. The transfer curve (I_d versus V_{gs}) in PBS using the functionalized Au gate electrode prior to the protein detection was used as the baseline signal (I_0). The same Au gate electrode was afterward incubated with a solution containing the protein target for 30 min. This procedure was chosen as samples from patients can be processed in a very similar procedure. To obtain the analytical curve, we prepared multiple concentrations of the analyte and started the measurements from the most diluted one. The normalized response (in %) of the sensor was calculated according to eq 1:

$$\frac{\Delta I}{I_0} (\%) = 100 \times \frac{I_d - I_0}{I_0} \quad (1)$$

The LOD was calculated using eq 2 defined by the International Union of Pure and Applied Chemistry:^{21,29}

$$\text{LOD} = 10 \frac{\left(\frac{\Delta I}{I_0} \right)_{\text{blank}} + 3 \times \sigma}{A} - B \quad (2)$$

where $(\Delta I/I_0)_{\text{blank}}$ is the average drain current variation of a blank sample (reference). Here, we used the average variation from the BSA specificity test (2.5%, see Figure 3e) to avoid false positive results. σ is the relative standard deviation (0.5%), and A and B are the intercept and slope of the analytical curve, respectively, and can be found in Figure S10.

Electrochemical Characterization. The electrochemical impedance spectroscopy (EIS) was performed in a three-electrode configuration using a potentiostat (PlamSens4). The source and drain electrodes were shorted and served as the working electrode. A Ag/AgCl pellet was utilized as the reference electrode, while a Pt electrode acted as the counter electrode. EIS measurements were performed in open circuit conditions (OCP) (10 kHz to 0.5 Hz, Eac 10 mV). For the measurements of Au functionalization steps, the PBS solution was added of 5 mM $[\text{Fe}(\text{CN})_6]^{3-/4-}$.

Quartz Crystal Microbalance with Dissipation Monitoring (QCM-D). QCM-D was used to monitor the frequency (Δf) changes after the antibodies' attachment on the Au surface. The experiments

were performed by using a Q-Sense Explorer single module system from Biolin Scientific (Gothenburg, Sweden). First the Au crystal was cleaned with a 1:1 (v/v) solvent mixture (acetone/isopropyl alcohol) in a sonication bath. The cleaned crystal was immersed in the 11MUA (10 mM) ethanol solution overnight to allow the formation of a self-assembled monolayer (SAM) with functional carboxylic groups. Then, the crystal was inserted into the QCM-D and the monolayer was activated in a mixed solution of EDC (20 mM) and NHS (10 mM) in MES for 30 min in flux ($25 \mu\text{L min}^{-1}$). The crystal with the activated monolayer was stabilized in a PBS solution. Subsequently, a flow of antibody solution (10^{-8} M in PBS solution) was introduced at a rate of $25 \mu\text{L min}^{-1}$ for 10 min. Then, the flow was stopped for 20 min to allow all present antibodies to bind to the surface. This procedure was repeated three times. Finally, a PBS solution was flowed for 20 min to remove any nonbinding material from the crystal's surface. Lastly, to block remaining nonspecific binding sites of the Au electrode, a BSA solution (10 mg mL^{-1}) was flowed ($25 \mu\text{L min}^{-1}$) for 30 min. All QCM-D measurements were performed at room temperature. In the experiments, the resonance frequency and energy dissipation were measured at different harmonics ($n = 1, 3, 5, 7, 9, 11,$ and 13). Data were analyzed using QTools software, and the mass of bind antibodies was estimated using the viscoelastic model.³⁰

X-ray Photoelectron Spectroscopy (XPS). XPS measurements were carried out with a Kratos Axis Ultra DLD photoelectron spectrometer in a UHV chamber with a base pressure of 10^{-10} mbar, using a hemispherical analyzer and a monochromated Al $K(\alpha)$ source at 15 kV voltage bias and 10 mA emission current. The source line width is approximately 1.0 eV fwhm, as calibrated by the Ag $3d_{5/2}$ line. Spectra were collected using hybrid mode with an analysis area of $700 \mu\text{m} \times 300 \mu\text{m}$ (i.e., X-ray spot size). Spectra were measured at a takeoff angle of 0° regarding the sample surface normal. Survey spectra were measured with a pass energy of 80 eV and elemental spectra were measured with a pass energy of 20 eV.

RESULTS AND DISCUSSION

OECTs offer the advantage that various device architectures can be realized including suspended gate electrodes above the channel as well as an integrated planar configuration.^{10,31,32} Here, we used OECTs (Figure 1a), with patterned planar gate electrodes next to the source and drain contacts. The devices are based on PEDOT:PSS and were fabricated on glass substrates using a standard microfabrication procedure.³² The detailed process is presented in the Experimental Section. All devices herein consist of channel dimensions of $1 \times 0.3 \text{ mm}$ (width, $W \times$ length, L), with an average thickness of $55 \pm 5 \text{ nm}$, and a gate electrode with a diameter of 4 mm. PEDOT:PSS-based OECTs operate in a depletion mode. When a positive gate bias is applied, cations are injected from the electrolyte into the channel and dedoped onto the PEDOT:PSS, leading to a decrease in the drain current. The respective output and transfer characteristics of a planar OECT operated in PBS solution are shown in Figure 1b,c. A positive gate bias leads to a decrease in the drain current. The ability of an OECT to amplify a signal at the gate electrode can be evaluated using transconductance, which is calculated from the first derivative of the transfer curves (Figure 1b-blue line). Our devices reach a maximum peak transconductance of 4.36 mS for a $V_{\text{ds}} = -0.4 \text{ V}$ and $V_{\text{gs}} = 0.2 \text{ V}$, which is expected considering the geometry and active layer used.³³

For biosensing applications, device stability is crucial since any kind of degradation can potentially cause baseline drain current drifts, which would impair accurate analyte measurements. Figure 1d depicts the cycling stability of a planar OECT. First, the device underwent a precondition cycling as described in the Experimental Section, and then a series of transfer curves was consecutively measured for 50 cycles at a

fixed $V_{\text{ds}} = -0.4 \text{ V}$. The device demonstrated exceptional stability during continuous measurements, displaying only a slight drain current drift of 1.98% at $V_{\text{gs}} = 0 \text{ V}$. This stability makes them reliable transducers for biosensing applications.

Using electrochemical impedance spectroscopy (EIS), we determined the capacitance of the Au gate electrode and the PEDOT:PSS channel (see Figure 1e) to be 0.918 ± 0.003 and $0.47 \pm 0.05 \mu\text{F}$, respectively. Using the geometry of the channel, the volumetric capacitance of the PEDOT:PSS was calculated to be $30 \pm 3 \text{ F cm}^{-3}$, which is in agreement with the literature.³⁴

According to the Bernards and Malliaras model (eq 3), the drain current depends on the overall capacitance of the device.

$$I_{\text{d}} = \frac{G}{V_{\text{p}}} \left(V_{\text{p}} - V_{\text{eff}} + \frac{1}{2} V_{\text{d}} \right) V_{\text{d}} \quad (3)$$

$$G = \frac{WD}{L} q \mu \rho_0 \quad (4)$$

$$V_{\text{p}} = \frac{q \rho_0}{\nu} \quad (5)$$

$$V_{\text{eff}} = V_{\text{g}} \frac{C_{\text{o}}}{C_{\text{p}}} \quad (6)$$

$$C_{\text{o}} = \frac{C_{\text{g}} C_{\text{p}}}{C_{\text{g}} + C_{\text{p}}} \quad (7)$$

where G is the conductance of the channel, W is the width, D is the thickness, L is the length, q is electronic charge, μ is the hole mobility, ρ_0 is the initial hole density in the organic semiconductor before the application of a gate voltage, V_{p} is the pinch off voltage, C_{o} is the overall capacitance of the OECT, ν is the volume of the channel, V_{eff} is the effective gate voltage, C_{p} is the PEDOT:PSS capacitance, and C_{g} is the Au capacitance. In our case, the overall capacitance of the device is composed by the double layer capacitance of the Au gate electrode in series with the volumetric capacitance of the PEDOT:PSS film.³⁵ Typically, the gate electrode is designed in such a way that the gate capacitance is significantly higher than the channel capacitance. This way the modulation of the drain current solely depends on the channel's capacitance; since then, the C_{o} equals approximately C_{p} (eq 7). However, in our study, we aim to detect the analyte at the gate electrode's surface. Therefore, we have strategically designed OECTs with gate and channel capacitances in the same order of magnitudes to increase the device's sensitivity to changes in the gate capacitance.²⁹

The strategy adopted here to functionalize the Au gate electrode was to attach the bioreceptor SARS-CoV-2 spike Ab immunoglobulin G (IgG) to the Au surface. IgG antibodies, which are approximately 150 kDa in molecular mass and have dimensions of about $14 \text{ nm} \times 10 \text{ nm} \times 4 \text{ nm}$, are biopolymers composed of amino acids, similar to other proteins. They consist of two fragment antigen binding (Fab) regions and a fragment crystallizable region (Fc). For ideal immobilization, the antibody should be oriented in an "end-on" configuration, where the Fc region binds with the substrate while the Fab region remains free to bind with the antigen.³⁶ For the antibody immobilization, first, the gold surface was functionalized with a self-assembled monolayer (SAM) of 11-mercaptoundecanoic acid (11MUA). The thiol headgroup

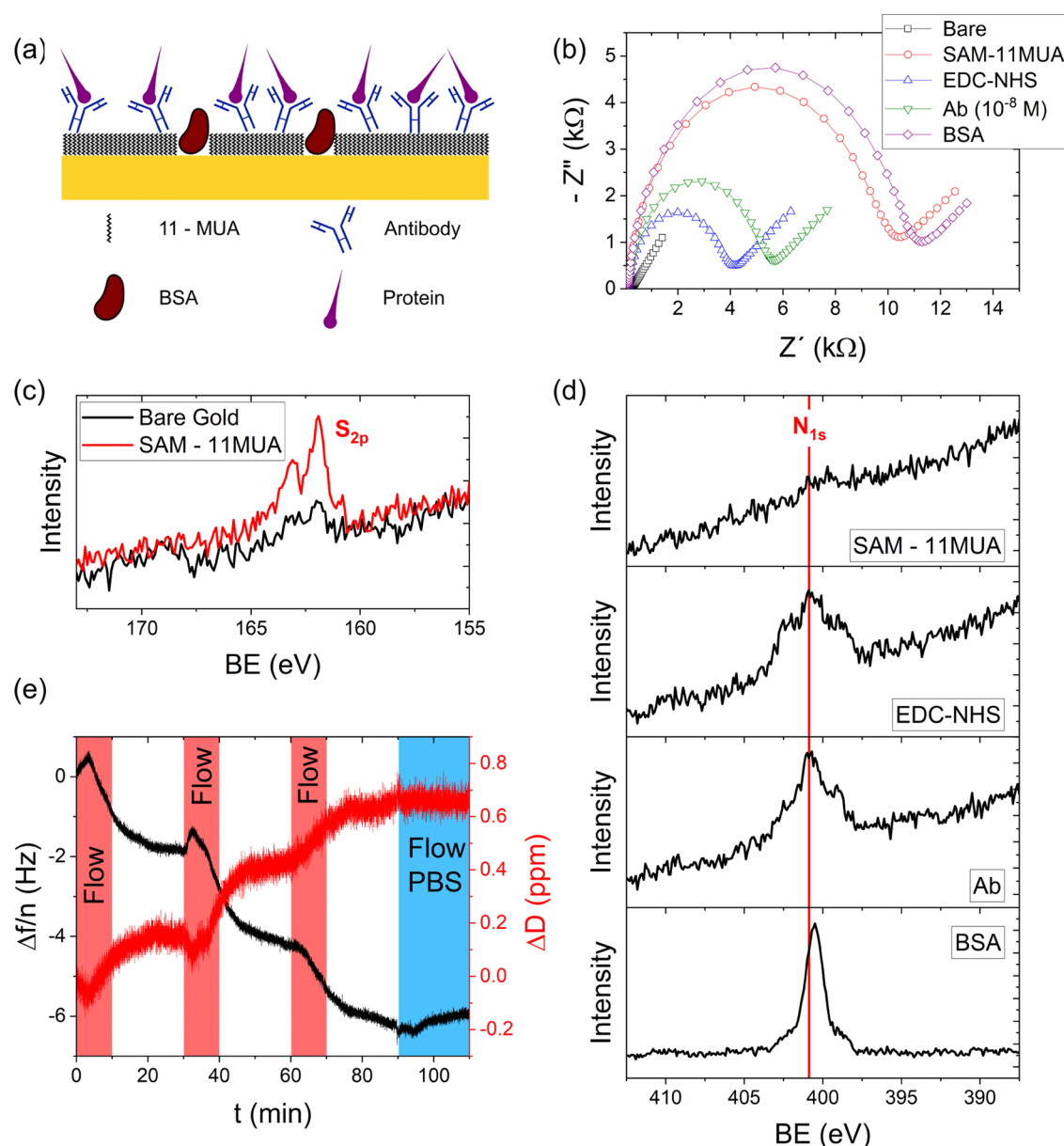


Figure 2. (a) Sketch of the functionalized Au gate electrode. (b) Nyquist plot in PBS solution containing 5 mM $[\text{Fe}(\text{CN})_6]^{3-/4-}$ using: bare Au (black square), Au/11MUA (red circle), Au/11MUA/EDC-NHS (blue triangle), Au/11MUA/EDC-NHS/Ab (green down-pointing triangle), and Au/11MUA/EDC-NHS/Ab/BSA (purple diamond). (c) High-resolution X-ray photoelectron spectroscopy (XPS) spectra of sulfur 2p (S_{2p}) on bare Au (black line) and Au/11MUA (red line). (d) High-resolution XPS spectra of nitrogen 1s (N_{1s}) Au/11MUA, Au/11MUA/EDC-NHS, Au/11MUA/EDC-NHS/Ab, and Au/11MUA/EDC-NHS/Ab/BSA. (e) Real-time QCM-D frequency and dissipation shift during the attachment of the antibodies for the first overtone ($n = 3$).

was chosen for the formation of stable covalent bonds to the Au gate electrodes.³⁷ The functional carboxylic groups of the SAM were then activated in order to form a covalent bond with the amine groups of the antibodies. According to Bhadra and co-workers, *n*-alkanethiol molecules with longer alkane chains ($n = 11$) form SAMs with denser packing, which favors end-on orientation of the antibodies, resulting in a greater efficiency of the antigen binding.³⁸ Finally, we used BSA to prevent nonspecific binding by blocking potentially uncovered Au surface with adsorbed albumin.

Figure 2a presents a sketch of the functionalized Au gate electrode, showing the antibody–protein couple. Figure 2b presents the Nyquist plot of the (functionalized) Au gate electrode acquired in a PBS solution with a redox probe. The

change in the impedance is caused by the modification of the surface: The formation of the SAM using 11MUA hinders the charge transfer between the Au and the electrolyte since both redox probe and 11MUA SAM are negatively charged.³⁹ In that way, the SAM works as an insulating layer, which results in a significant increase of the impedance. Activation of the SAM using the couple *N*-(3-(dimethylamino)propyl)-*N'*-ethyl-carbodiimide (EDC) and *N*-hydroxysuccinimide (NHS) yields an ester that decreases the amount of charges at the SAM, lowering the impedance, which justifies the observed result.⁴⁰ The immobilization of the antibody and blocking agent BSA increases the impedance by inducing an electronic insulation of the electrode that, in turn, prevents charge transfer.

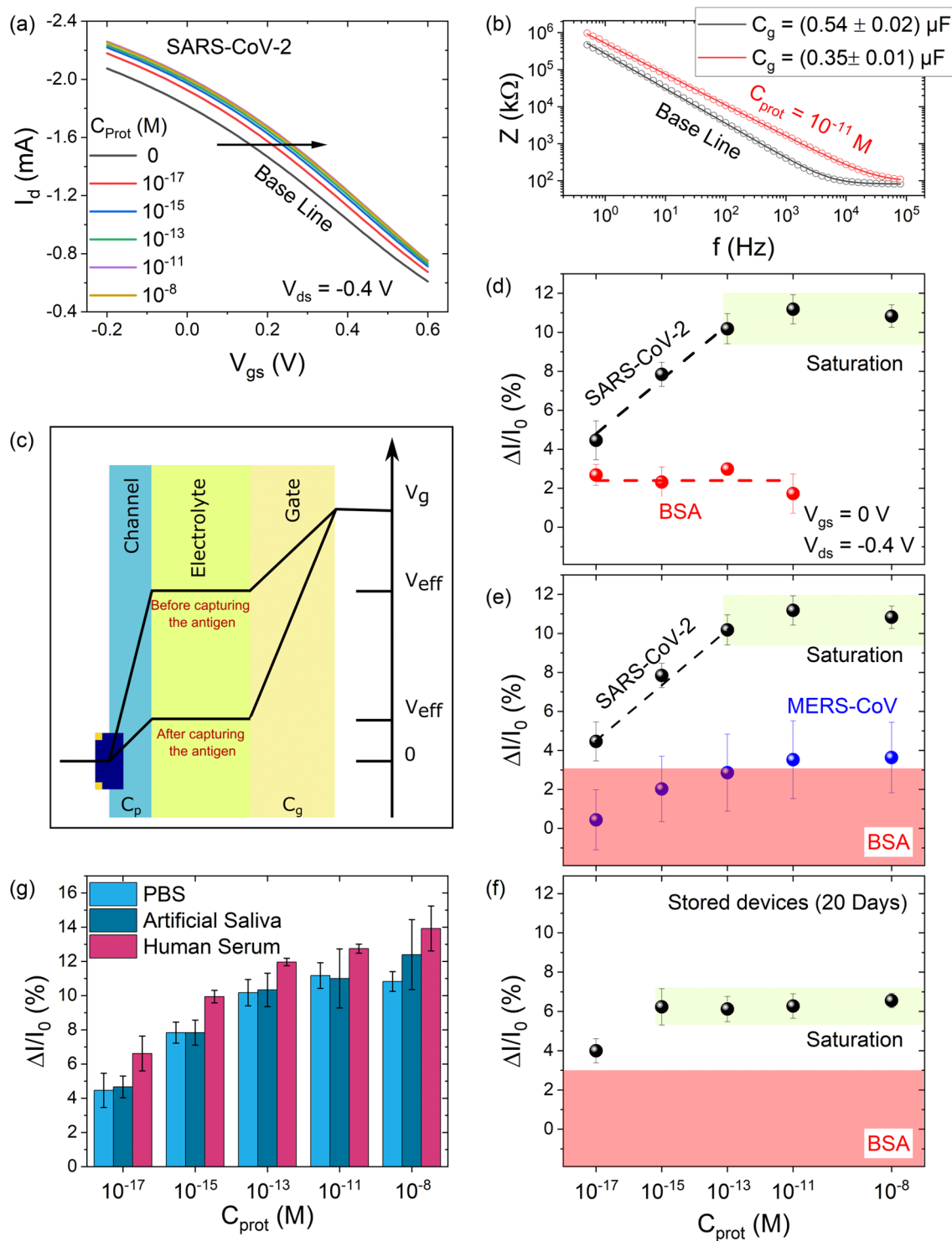


Figure 3. (a) Transfer curves of the sensor assayed with different concentrations of SARS-CoV-2 spike protein diluted in PBS solution. (b) Electrochemical impedance spectroscopy for a device before and after capturing the antigen. (c) Schematic diagram of potential drops at the interface gate/electrolyte and electrolyte/channel, in the OECT before and after capturing the antigen. (d) Analytical curve of the OECT-based immunosensor assayed with different concentrations of SARS-CoV-2 spike protein (black dots) and with BSA (red dots) demonstrating specificity of the sensor. The black line is the linear behavior of the analytical curve, and the red line is a guide for the eye. The green box indicates the saturation of the sensor. (e) Comparison between the analytical curve of the OECT-based immunosensor assayed with different concentrations of SARS-CoV-2 spike protein (black dots) and MERS-CoV spike protein (blue dots). The red region indicates the response for devices assayed with BSA. (f) Long-term stability: analytical curve of the OECT-based immunosensor (after 20 days) assayed with different concentrations of SARS-CoV-2 spike protein (black dots). The red region indicates the response for devices assayed with BSA. (g) Comparison of drain current variation for SARS-CoV-2 spike protein diluted in PBS (light blue), artificial saliva (dark blue), and human serum (pink). The transfer curves of the immunosensors assayed with artificial saliva and human serum can be found in Figures S11 and S12, respectively.

Furthermore, X-ray photoelectron spectroscopy (XPS) indicates the completion of each step of the Au gate electrode functionalization: Figure 2c shows the high-resolution spectra for bare Au (black line) and Au/11MUA (red line). As expected, the XPS spectra reveal the presence of S 2p following the functionalization of the Au electrode with the 11MUA SAM. Figure 2d depicts the high-resolution spectra for the respective functionalization Au/11MUA, Au/11MUA/EDC-NHS, Au/11MUA/EDC-NHS/Ab, and Au/11MUA/EDC-NHS/Ab/BSA. Here, we tracked the presence of N 1s on the samples surface since EDC-NHS, antibodies, and BSA all contain nitrogen species. After the activation of the 11MUA SAM, a peak emerges, confirming successful functionalization with EDC-NHS. Upon attachment of the antibodies, there is only a small change in the peak (see Figure S1 for a better comparison), rendering the results inconclusive. Finally, upon employing the blocking agent bovine serum albumin (BSA), a significant change in the intensity and position of the peak is observed, confirming the completion of the final step.

To further investigate and confirm the antibodies' attachment, we conducted real-time quartz crystal microbalance with dissipation monitoring (QCM-D) measurements. In the experiment, the gold sensor with the activated monolayer was first stabilized in a PBS solution. Subsequently, a flow of antibody solution (10^{-8} M in PBS solution) was introduced at a rate of $25 \mu\text{L min}^{-1}$ for 10 min (Figure 2e—red region), followed by a 20 min incubation time with stopped flow (Figure 2e—white region) to ensure sufficient time for covalent bonds to form. This cycle was repeated three times to reach an amount of antibodies that is sufficient for reliable detection. Finally, a PBS solution was flowed for 20 min (Figure 2e—blue region) to remove any nonbinding material from the crystal's surface. The graph in Figure 2e shows a total decrease in the resonance frequency by -5.8 Hz after the three incubation steps and a slight increase in the dissipation energy equal to 0.65 ppm for the first overtone, $n = 3$. Figure S2a,b shows all recorded harmonics for resonance frequency and dissipation energy. The decreasing resonance frequency indicates the deposition of material on the surface of the quartz crystal, in our case, the attachment of the antibodies. Remarkably, no notable frequency shift was detected during the last flushing step with PBS, indicating a strong attachment of the antibodies to the surface, which can be attributed to the formation of covalent bonds between the antibodies and the SAM, ensuring a stable and reliable connection. Furthermore, the variation in dissipation, ΔD , offers insights into the mechanical properties of the adsorbed layer, such as its softness or viscoelasticity. In our case, ΔD is very small, which we attribute to the fact that the quartz surface was not fully covered by proteins. As the overtones were spreading slightly (Figure S2a) and the protein adsorption usually results in soft films, we applied a viscoelastic model (Figure S2c) to quantify the mass per area of the antibodies attached on the crystal surface.^{30,41} According to this model, the total mass was determined to be 2.7×10^{-8} g (Figure S2d), corresponding to approximately 1.08×10^{11} antibodies attached to the surface. We can theoretically estimate the number of antibodies expected to cover the entire surface using the average size of the antibodies: For 100% coverage of the crystal, we would expect the number of antibodies to be between 1.4×10^{11} and 5×10^{11} depending on their orientation ("lying-on" versus end-on). Hence, we estimate a coverage between 22 and 77%. Although our functionalization strategy favors end-on

orientation, we still expect a mixture of possible antibody orientations.

Additional details on the functionalization of the Au gate electrode surface can be found in the Supporting Information. Figure S4 presents the cyclic voltammetry in PBS solution with the redox probe for the bare Au and the Au surface covered with SAM. As expected, after the SAM formation, the redox peaks disappear in agreement with impedance spectroscopy data (Figure 2b). Figure S3 presents the QCM-D measurement for SAM activation with the EDC-NHS and the attachment of the blocking agent BSA. Both results show a decrease in the resonance frequency of the quartz crystal, indicating the successful attachment of the respective materials on the surface. Moreover, Figure S5 displays the water contact angle measurements conducted after each functionalization step, confirming the modification of the electrode surface. This set of complementary characterizations substantiates the success of the adopted protocol to functionalize the Au gate electrode surface.

Figure 3a presents the response of an OECT-based sensor (transfer characteristics) in dependence of different SARS-CoV-2 spike protein concentrations. For comparison, the response of several additional sensors can be found in Figure S6. Figure 3a displays a shift of the transfer curve toward higher gate voltages as the concentration increases. According to the Bernards–Malliaras model (eq 3), this shift is attributed to a decrease in the overall capacitance of the device. Indeed, the fitting of the impedance modulus for a functionalized Au gate electrode, before and after being assayed with a 10^{-11} M solution of the Sars-CoV-2 spike protein, shows a decrease in the electrode capacitance. The presented results in Figure 3b demonstrate that the initial capacitance was measured to be $0.54 + 0.02 \mu\text{F}$ and decreased to $0.35 + 0.02 \mu\text{F}$ after the assay. The sensing mechanism is visualized in the scheme in Figure 3c. A lower gate capacitance implies a reduction of V_{eff} due to the higher voltage dropping at the interface gate/electrolyte. Consequently, to accumulate the same number of ions within the channel and achieve an equivalent level of dedoping in the PEDOT:PSS, a higher gate voltage is required.

Figure 3d presents the analytical curve of the immunosensors and depicts the variation of the drain current in relation to the baseline ($C_{\text{prot}} = 0$ M) for different spike protein (black dots) and BSA (red dots) concentrations. Based on the stability test (Figure 1d), $V_{\text{gs}} = 0$ V (smallest drain current drift) was chosen to ensure a very high reliability of the sensor results. The drain current variation increases linearly with the spike protein concentration until a concentration of 10^{-13} M. After this point, the sensor reaches a saturation state (green box in Figure 3d). This saturation indicates that there are no more free antibody sites to which the spike proteins bind to. At this point, it is important to keep in mind that when it comes to COVID-19 sensors, a very critical factor is the LOD. The LOD determines the lowest concentration of the virus that can be reliably detected by the respective sensor. While a broad linear dynamic range is advantageous in various sensing applications, it is not as essential to detect viruses, such as SARS-CoV-2. The primary requirement is that the sensor can accurately determine whether a sample is positive or negative for the viruses even at low concentrations. The LOD for the SARS-CoV-2 sensor has been calculated using eq 2 (Experimental Section) and was determined to be as low as 10^{-17} M. This LOD value places the sensor among the best in its category, specifically among organic transistor-based sensors

for detecting SARS-CoV-2.^{24,42–48} The impressive LOD indicates the sensor's high sensitivity and ability to detect extremely low concentrations, enhancing its reliability and effectiveness in identifying positive or negative samples. The incubation time adopted here was 30 min, which is similar to the conventional "quick antigen test".

As a control experiment, we tested the device using various concentrations of BSA diluted in a PBS solution (Figure 3d with red dots). Since BSA features high adhesive strength, but no specific interactions with the antibodies, this experiment aims to confirm the specificity of the sensor (no significant transfer curve shift is expected). The transfer curves of the immunosensors assayed with BSA can be found in Figure S7. The obtained results confirm that even when the sensor is assayed with a highly concentrated BSA solution (10^{-11} M), no notable response is observed. We conducted an additional specificity test using the spike protein from MERS-CoV, which belongs to the same family, order, and genus as SARS-CoV-2.⁴⁹ The transfer curves of the immunosensors assayed with MERS-CoV can be found in Figure S8. The analytical curve in Figure 3e shows that the sensors present a minimum drain current variation, reaching a maximum of $(4 \pm 2)\%$ at the highest concentration (10^{-8} M). The results indicate that the sensor is specific in its detection, even in the presence of closely related and adhesive analytes at a high concentration.

In order to assess the stability of the sensors for potential implementation as a POC device, the functionalized sensors were stored at 4 °C in a refrigerator for a duration of 20 days. To investigate any potential changes in the electrical properties of the sensor, transfer curves were obtained both before and after the storage period (Figure S9). Remarkably, no significant changes were observed in the transfer characteristics, indicating the absence of any notable change in the electrical properties of either the PEDOT:PSS film or the functionalized Au gate electrode. Subsequently, the stored devices were tested with different concentrations of a SARS-CoV-2 spike protein solution. The transfer curve obtained after testing with a solution at the LOD concentration is represented by the red line in Figure S9. The device exhibited a clear shift to higher gate voltages, similar to the case for the fresh devices. In Figure 3f, the analytical curve further demonstrates that the LOD of the devices remained the same during 20 days of storage. The only noticeable change is the point of saturation, which shifted from a concentration of 10^{-13} to 10^{-15} M. However, as previously discussed, the most crucial parameter for SARS-CoV-2 sensors is the LOD, which remained unchanged. In brief, even after the storage period, the sensors maintained their ability to detect and respond to the target analyte with a consistent and comparable performance to the fresh devices. Lastly, to showcase the effectiveness of the proposed sensor in practical scenarios, the devices were incubated using SARS-CoV-2 protein diluted in artificial saliva and human serum, which are biofluids capable of mimicking the complexity of real-world samples. Figure 3g shows that in both cases the sensor's LOD remains consistent with that obtained when the protein was detected in PBS, alongside a similar drain current variation. These findings demonstrate the robustness, stability, and sensitivity of the sensor, affirming the potential for implementations as POC devices.

CONCLUSIONS

We introduced a label-free electrochemical immunosensor for the rapid and highly sensitive detection of the SARS-CoV-2

spike protein. The platform utilizes PEDOT:PSS-based OECTs as a transducer. The planar Au gate electrode of the OECTs is functionalized with SARS-CoV-2 antibodies, enabling the specific capture of the SARS-CoV-2 spike protein through antibody–antigen interactions. When the antigen is captured, it leads to a decrease in the gate capacitance, resulting in a corresponding decrease in the effective gate voltage. This change is reflected in a shift in the transfer curve to higher gate voltages. The limit of detection (LOD) reaches an impressive concentration of 10^{-17} M in aqueous PBS, artificial saliva, and human serum solutions. Additionally, the device exhibits high specificity when tested with BSA and MERS-CoV, showing only a small response (less than 4%) at high concentrations. Furthermore, the OECTs demonstrate excellent stability during storage for 20 days, ensuring reliability and practicality for applications as a point-of-care (POC) device. Finally, the platform allows easy adaptation, and the same general approach can be applied to detect and analyze various other pathogens or biomarkers enabling a broad range of applications.

ASSOCIATED CONTENT

Supporting Information

The Supporting Information is available free of charge at <https://pubs.acs.org/doi/10.1021/acsaelm.4c00260>.

XPS spectra of N 1s for a sample covered with EDS-NHS and a sample with antibodies, QCM-D results for the antibodies attachment step; cyclic voltammetry for bare gold and gold covered with the monolayer (11MUA); water contact angles for all of the steps of gold functionalization; transfer curves of all OECT-based sensors tested; and analytical curve of the sensor with the fitting for LOD calculation (PDF)

AUTHOR INFORMATION

Corresponding Authors

Renan Colucci – Organic Bioelectronics Research Group, Max Planck Institute for Polymer Research, 55128 Mainz, Germany; orcid.org/0000-0002-0669-9823; Email: coluccir@mpip-mainz.mpg.de

Ulrike Kraft – Organic Bioelectronics Research Group, Max Planck Institute for Polymer Research, 55128 Mainz, Germany; Email: kraftu@mpip-mainz.mpg.de

Authors

Dimitrios A. Koutsouras – Department of Molecular Electronics, Max Planck Institute for Polymer Research, 55128 Mainz, Germany; IMEC NL, 5656 AE Eindhoven, The Netherlands

Svenja Morsbach – Department of Physical Chemistry of Polymers, Max Planck Institute for Polymer Research, 55128 Mainz, Germany; orcid.org/0000-0001-9662-8190

Paschalis Gkoupidenis – Department of Molecular Electronics, Max Planck Institute for Polymer Research, 55128 Mainz, Germany; orcid.org/0000-0002-0139-0851

Paul W. M. Blom – Department of Molecular Electronics, Max Planck Institute for Polymer Research, 55128 Mainz, Germany; orcid.org/0000-0002-6474-9497

Complete contact information is available at: <https://pubs.acs.org/doi/10.1021/acsaelm.4c00260>

Author Contributions

R.C.: conceptualization, methodology, investigation, data analysis, and writing—original draft. D.A.K.: data analysis, methodology, and writing—original draft. S.M.: QCM-D conceptualization, QCM-D data analysis, and writing—review of the final version. P.G.: OECT fabrication conceptualization, OECT data analysis, and writing—review of the final version. P.W.M.B.: methodology, data analysis, and writing—review of the final version. U.K.: conceptualization, methodology, supervision, data analysis, funding acquisition, and writing—original draft. All authors have given approval to the final version of the manuscript.

Funding

Open access funded by Max Planck Society.

Funding

Volkswagen foundation AZ.: 98 436 Recipient: Ulrike Kraft.

Notes

The authors declare no competing financial interest.

ACKNOWLEDGMENTS

The authors thank the VW-foundation under the call “Corona Crisis and Beyond” for funding and Leon Prädél from the Department of Molecular Spectroscopy at Max Planck Institute for Polymer Research for conducting the XPS measurements.

REFERENCES

- (1) Cucinotta, D.; Vanelli, M. WHO Declares COVID-19 a Pandemic. *Acta Bio Med. Atenei Parmensis* **2020**, *91* (1), 157.
- (2) Bustin, S. A.; Nolan, T. RT-QPCR Testing of SARS-COV-2: A Primer. *Int. J. Mol. Sci.* **2020**, *21* (8), 304.
- (3) Gong, F.; Wei, H. X.; Li, Q.; Liu, L.; Li, B. Evaluation and Comparison of Serological Methods for COVID-19 Diagnosis. *Front. Mol. Biosci.* **2021**, *8*, 683.
- (4) Stakenborg, T.; Raymenants, J.; Taher, A.; Marchal, E.; Verbruggen, B.; Roth, S.; Jones, B.; Yurt, A.; Duthoo, W.; Bombeke, K.; Fauvart, M.; Verplanken, J.; Wiederkehr, R. S.; Humbert, A.; Dang, C.; Vlassaks, E.; Jáuregui Uribe, A. L.; Luo, Z.; Liu, C.; Zinoviev, K.; Labie, R.; Frederiks, A. D.; Saldien, J.; Covens, K.; Berden, P.; Schreurs, B.; Van Duppen, J.; Hanifa, R.; Beuscart, M.; Pham, V.; Emmen, E.; Dewagtere, A.; Lin, Z.; Peca, M.; El Jerrari, Y.; Nawghane, C.; Arnett, C.; Lambrechts, A.; Deshpande, P.; Lagrou, K.; De Munter, P.; André, E.; Van den Wijngaert, N.; Peumans, P. Molecular Detection of SARS-COV-2 in Exhaled Breath at the Point-of-Need. *Biosens. Bioelectron.* **2022**, *217*, No. 114663.
- (5) Scohy, A.; Anantharajah, A.; Bodéus, M.; Kabamba-mukadi, B.; Verroken, A.; Rodriguez-villalobos, H. Low Performance of Rapid Antigen Detection Test as Frontline Testing for COVID-19 Diagnosis. *J. Clin. Virol.* **2020**, *129*, No. 104455.
- (6) Guglielmi, G. Rapid Coronavirus Tests: A Guide for the Perplexed. *Nature* **2021**, *590* (7845), 202–205.
- (7) Prabowo, B. A.; Cabral, P. D.; Freitas, P.; Fernandes, E. The Challenges of Developing Biosensors for Clinical Assessment: A Review. *Chemosensors* **2021**, *9* (11), 299.
- (8) Bai, L.; Elósegui, C. G.; Li, W.; Yu, P.; Fei, J.; Mao, L. Biological Applications of Organic Electrochemical Transistors: Electrochemical Biosensors and Electrophysiology Recording. *Front. Chem.* **2019**, *7*, No. e1805813.
- (9) Marks, A.; Griggs, S.; Gasparini, N.; Moser, M. Organic Electrochemical Transistors: An Emerging Technology for Biosensing. *Adv. Mater. Interfaces* **2022**, *9* (6), No. 2102039.
- (10) Colucci, R.; Barbosa, H. F. D. P.; Günther, F.; Cavassin, P.; Faria, G. C. Recent Advances in Modeling Organic Electrochemical Transistors. *Flexible Printed Electron.* **2020**, *5* (1), No. 013001.
- (11) Ohayon, D.; Druet, V.; Inal, S. A Guide for the Characterization of Organic Electrochemical Transistors and Channel Materials. *Chem. Soc. Rev.* **2023**, *52* (3), 1001–1023.
- (12) Torricelli, F.; Adrahtas, D. Z.; Bao, Z.; Berggren, M.; Biscarini, F.; Bonfiglio, A.; Bortolotti, C. A.; Frisbie, C. D.; Macchia, E.; Malliaras, G. G.; McCulloch, I.; Moser, M.; Nguyen, T. Q.; Owens, R. M.; Salleo, A.; Spanu, A.; Torsi, L. Electrolyte-Gated Transistors for Enhanced Performance Bioelectronics. *Nat. Rev. Methods Primers* **2021**, *1* (1), 66.
- (13) Bidinger, S. L.; Han, S.; Malliaras, G. G.; Hasan, T. Highly Stable PEDOT:PSS Electrochemical Transistors. *Appl. Phys. Lett.* **2022**, *120* (7), No. 073302.
- (14) Hu, J.; Wei, W.; Ke, S.; Zeng, X.; Lin, P. A Novel and Sensitive Sarcosine Biosensor Based on Organic Electrochemical Transistor. *Electrochim. Acta* **2019**, *307*, 100–106.
- (15) Diacci, C.; Lee, J. W.; Janson, P.; Dufil, G.; Méhes, G.; Berggren, M.; Simon, D. T.; Stavrinidou, E. Real-Time Monitoring of Glucose Export from Isolated Chloroplasts Using an Organic Electrochemical Transistor. *Adv. Mater. Technol.* **2020**, *5* (3), No. 1900262.
- (16) Demuru, S.; Huang, C. H.; Parvez, K.; Worsley, R.; Mattana, G.; Piro, B.; Noël, V.; Casiraghi, C.; Briand, D. All-Inkjet-Printed Graphene-Gated Organic Electrochemical Transistors on Polymeric Foil as Highly Sensitive Enzymatic Biosensors. *ACS Appl. Nano Mater.* **2022**, *5* (1), 1664–1673.
- (17) Koklu, A.; Wustoni, S.; Musteata, V. E.; Ohayon, D.; Moser, M.; McCulloch, I.; Nunes, S. P.; Inal, S. Microfluidic Integrated Organic Electrochemical Transistor with a Nanoporous Membrane for Amyloid- β Detection. *ACS Nano* **2021**, *15* (5), 8130–8141.
- (18) Ji, X.; Lin, X.; Rivnay, J. Organic Electrochemical Transistors as On-Site Signal Amplifiers for Electrochemical Aptamer-Based Sensing. *Nat. Commun.* **2023**, *14* (1), No. 1665.
- (19) Méhes, G.; Roy, A.; Strakosas, X.; Berggren, M.; Stavrinidou, E.; Simon, D. T. Organic Microbial Electrochemical Transistor Monitoring Extracellular Electron Transfer. *Adv. Sci.* **2020**, *7* (15), No. 2000641.
- (20) Vizzini, P.; Beltrame, E.; Coppedè, N.; Vurro, F.; Andreatta, F.; Torelli, E.; Manzano, M. Detection of *Listeria Monocytogenes* in Foods with a Textile Organic Electrochemical Transistor Biosensor. *Appl. Microbiol. Biotechnol.* **2023**, *107*, 3789–3800.
- (21) Guo, K.; Wustoni, S.; Koklu, A.; Díaz-Galicia, E.; Moser, M.; Hama, A.; Alqahtani, A. A.; Ahmad, A. N.; Alhamlan, F. S.; Shuaib, M.; Pain, A.; McCulloch, I.; Arold, S. T.; Grünberg, R.; Inal, S. Rapid Single-Molecule Detection of COVID-19 and MERS Antigens via Nanobody-Functionalized Organic Electrochemical Transistors. *Nat. Biomed. Eng.* **2021**, *5* (7), 666–677.
- (22) Decataldo, F.; Giovannini, C.; Grumiro, L.; Marino, M. M.; Faccin, F.; Brandolini, M.; Dirani, G.; Taddei, F.; Lelli, D.; Tessarolo, M.; Calienni, M.; Cacciotto, C.; De Pascali, A. M.; Lavazza, A.; Fraboni, B.; Sambri, V.; Scagliarini, A. Organic Electrochemical Transistors as Versatile Tool for Real-Time and Automated Viral Cytopathic Effect Evaluation. *Viruses* **2022**, *14* (6), 1155.
- (23) Sensi, M.; Migatti, G.; Beni, V.; D’Alvise, T. M.; Weil, T.; Berto, M.; Greco, P.; Imbriano, C.; Biscarini, F.; Bortolotti, C. A. Monitoring DNA Hybridization with Organic Electrochemical Transistors Functionalized with Polydopamine. *Macromol. Mater. Eng.* **2022**, *307* (5), No. 2100880.
- (24) Liu, H.; Yang, A.; Song, J.; Wang, N.; Lam, P.; Li, Y.; Law, H. K. W.; Yan, F. Ultrafast, Sensitive, and Portable Detection of COVID-19 IgG Using Flexible Organic Electrochemical Transistors. *Sci. Adv.* **2021**, *7* (38), No. eabg8387.
- (25) Koutsouras, D. A.; Amiri, M. H.; Blom, P. W. M.; Torricelli, F.; Asadi, K.; Gkoupidenis, P. An Iontronic Multiplexer Based on Spatiotemporal Dynamics of Multiterminal Organic Electrochemical Transistors. *Adv. Funct. Mater.* **2021**, *31* (22), No. 2011013.
- (26) Brazaca, L. C.; Imamura, A. H.; Gomes, N. O.; Almeida, M. B.; Scheidt, D. T.; Raymundo-Pereira, P. A.; Oliveira, O. N.; Janegitz, B. C.; Machado, S. A. S.; Carrilho, E. Electrochemical Immunosensors Using Electrodeposited Gold Nanostructures for Detecting the S

- Proteins from SARS-CoV and SARS-CoV-2. *Anal. Bioanal. Chem.* **2022**, *414* (18), 5507–5517.
- (27) Soares, J. C.; Soares, A. C.; Angelim, M. K. S. C.; Proença-Modena, J. L.; Moraes-Vieira, P. M.; Mattoso, L. H. C.; Oliveira, O. N., Jr. Diagnostics of SARS-CoV-2 Infection Using Electrical Impedance Spectroscopy with an Immunosensor to Detect the Spike Protein. *Talanta* **2022**, *239*, No. 123076.
- (28) Mehmandoust, M.; Gumus, Z. P.; Soylak, M.; Erk, N. Electrochemical Immunosensor for Rapid and Highly Sensitive Detection of SARS-CoV-2 Antigen in the Nasal Sample. *Talanta* **2022**, *240*, No. 123211.
- (29) Macchia, E.; Romele, P.; Manoli, K.; Ghittorelli, M.; Magliulo, M.; Kovács-Vajna, Z. M.; Torricelli, F.; Torsi, L. Ultra-Sensitive Protein Detection with Organic Electrochemical Transistors Printed on Plastic Substrates. *Flexible Printed Electron.* **2018**, *3* (3), No. 034002.
- (30) Voinova, M. V.; Rodahl, M.; Jonson, M.; Kasemo, B. Viscoelastic Acoustic Response of Layered Polymer Films at Fluid-Solid Interfaces: Continuum Mechanics Approach. *Phys. Scr.* **1999**, *59* (5), 391–396.
- (31) Rivnay, J.; Inal, S.; Salleo, A.; Owens, R. M.; Berggren, M.; Malliaras, G. G. Organic Electrochemical Transistors. *Nat. Rev. Mater.* **2018**, *3* (2), 17086.
- (32) Koutsouras, D. A.; Torricelli, F.; Gkoupidenis, P.; Blom, P. W. M. Efficient Gating of Organic Electrochemical Transistors with In-Plane Gate Electrodes. *Adv. Mater. Technol.* **2021**, *6* (12), No. 202100732.
- (33) Friedlein, J. T.; McLeod, R. R.; Rivnay, J. Device Physics of Organic Electrochemical Transistors. *Org. Electron.* **2018**, *63*, 398–414.
- (34) Rivnay, J.; Leleux, P.; Ferro, M.; Sessolo, M.; Williamson, A.; Koutsouras, D. A.; Khodagholy, D.; Ramuz, M.; Strakosas, X.; Owens, R. M.; Benar, C.; Badier, J.-M. J.-M.; Bernard, C.; Malliaras, G. G. High-Performance Transistors for Bioelectronics through Tuning of Channel Thickness. *Sci. Adv.* **2015**, *1* (4), No. e1400251.
- (35) Bernards, D. A.; MacAya, D. J.; Nikolou, M.; DeFranco, J. A.; Takamatsu, S.; Malliaras, G. G. Enzymatic Sensing with Organic Electrochemical Transistors. *J. Mater. Chem.* **2008**, *18* (1), 116–120.
- (36) Welch, N. G.; Scoble, J. A.; Muir, B. W.; Pigram, P. J. Orientation and Characterization of Immobilized Antibodies for Improved Immunoassays (Review). *Biointerphases* **2017**, *12* (2), No. 02D301.
- (37) Ulman, A. Formation and Structure of Self-Assembled Monolayers. *Chem. Rev.* **1996**, *96* (4), 1533–1554.
- (38) Bhadra, P.; Shajahan, M. S.; Bhattacharya, E.; Chadha, A. Studies on Varying N-Alkanethiol Chain Lengths on a Gold Coated Surface and Their Effect on Antibody-Antigen Binding Efficiency. *RSC Adv.* **2015**, *5* (98), 80480–80487.
- (39) Raymundo-Pereira, P. A.; De Oliveira Pedro, R.; Carr, O.; Melendez, M. E.; Gobbi, A. L.; Helena De Oliveira Piazzetta, M.; Carvalho, A. L.; Reis, R. M.; Miranda, P. B.; Oliveira, O. N. Influence of the Molecular Orientation and Ionization of Self-Assembled Monolayers in Biosensors: Application to Genosensors of Prostate Cancer Antigen 3. *J. Phys. Chem. C* **2021**, *125* (1), 498–506.
- (40) Garrote, B. L.; Santos, A.; Bueno, P. R. Perspectives on and Precautions for the Uses of Electric Spectroscopic Methods in Label-Free Biosensing Applications. *ACS Sens.* **2019**, *4* (9), 2216–2227.
- (41) Martínez-Negro, M.; Oberländer, J.; Simon, J.; Mailänder, V.; Morsbach, S.; Landfester, K. A New Methodology Combining QCM-D and Proteomic Profiling Enables Characterization of Protein Adsorption on 2D Surfaces. *J. Colloid Interface Sci.* **2023**, *630*, 965–972.
- (42) Seo, G.; Lee, G.; Kim, M. J.; Baek, S. H.; Choi, M.; Ku, K. B.; Lee, C. S.; Jun, S.; Park, D.; Kim, H. G.; Kim, S. J.; Lee, J. O.; Kim, B. T.; Park, E. C.; Kim, S. I. Rapid Detection of COVID-19 Causative Virus (SARS-CoV-2) in Human Nasopharyngeal Swab Specimens Using Field-Effect Transistor-Based Biosensor. *ACS Nano* **2020**, *14* (4), 5135–5142.
- (43) Li, Y.; Peng, Z.; Holl, N. J.; Hassan, M. R.; Pappas, J. M.; Wei, C.; Izadi, O. H.; Wang, Y.; Dong, X.; Wang, C.; Huang, Y. W.; Kim, D.; Wu, C. MXene-Graphene Field-Effect Transistor Sensing of Influenza Virus and SARS-CoV-2. *ACS Omega* **2021**, *6* (10), 6643–6653.
- (44) Song, Y.; Lamberty, Z. D.; Liang, J.; Aller Pellitero, M.; Wagner, J. S.; Jumai'an, E.; Bevan, M. A.; Frechette, J.; Arroyo-Currás, N.; Katz, H. E. Nanoscale Bioreceptor Layers Comprising Carboxylated Polythiophene for Organic Electrochemical Transistor-Based Biosensors. *ACS Appl. Nano Mater.* **2021**, *4* (12), 13459–13468.
- (45) Wang, X.; Kong, D.; Guo, M.; Wang, L.; Gu, C.; Dai, C.; Wang, Y.; Jiang, Q.; Ai, Z.; Zhang, C.; Qu, D.; Xie, Y.; Zhu, Z.; Liu, Y.; Wei, D. Rapid SARS-CoV-2 Nucleic Acid Testing and Pooled Assay by Tetrahedral DNA Nanostructure Transistor. *Nano Lett.* **2021**, *21* (22), 9450–9457.
- (46) Kang, H.; Wang, X.; Guo, M.; Dai, C.; Chen, R.; Yang, L.; Wu, Y.; Ying, T.; Zhu, Z.; Wei, D.; Liu, Y.; Wei, D. Ultrasensitive Detection of SARS-CoV-2 Antibody by Graphene Field-Effect Transistors. *Nano Lett.* **2021**, *21* (19), 7897–7904.
- (47) Cui, T.-R.; Qiao, Y.; Gao, J.; Wang, C.; Zhang, Y.; Han, L.; Yang, Y.; Ren, T. Ultrasensitive Detection of Covid-19 Causative Virus (Sars-Cov-2) Spike Protein Using Laser Induced Graphene Field-Effect Transistor. *Molecules* **2021**, *26* (22), 6947.
- (48) Fan, J.; Parr, S.; Kang, S.; Gupta, M. Point-of-Care (POC) SARS-CoV-2 Antigen Detection Using Functionalized Aerosol Jet-Printed Organic Electrochemical Transistors (OECTs). *Nanoscale* **2023**, *15* (11), 5476–5485.
- (49) Abdelrahman, Z.; Li, M.; Wang, X. Comparative Review of SARS-CoV-2, SARS-CoV, MERS-CoV, and Influenza A Respiratory Viruses. *Front. Immunol.* **2020**, *11*, 2909.